Coupling hemodynamics with mechanobiology in patient-specific computational models of ascending thoracic aortic aneurysms

S. Jamaleddin Mousavi, R. Jayendiran, S. Farzaneh, S. Campisi, M. Viallon, P. Croisille, S. Avril

Version of Record: https://www.sciencedirect.com/science/article/pii/S0169260721001826
Manuscript_8f69d1cfdfeac32749e729a56b836c3c

Coupling hemodynamics with mechanobiology in patient-specific computational models of ascending thoracic aortic aneurysms

S. Jamaleddin Mousavi [1,†], Raja Jayendiran [1,†], Solmaz Farzaneh[1], Salvatore Campisi[1,2], Magalie Viallon[3,4], Pierre Croisille[3,4] and Stéphane Avril[1*]

affiliations: [1]Mines Saint-Étienne, Univ Lyon, Univ Jean Monnet, INSERM, U1059 Sainbiose, F - 42023 Saint-Étienne France.
[2]University Hospital of Saint-Étienne, Department of Cardiovascular Surgery, Saint-Étienne cedex, France. [3] Université de Lyon, UJM-Saint-Etienne, INSA, CNRS UMR 5520, INSERM U1206, CREATIS, F-42023, Saint-Étienne, France. [4] University Hospital of Saint-Étienne, Department of Radiology, Saint-Étienne, France.

abbreviated title: Coupling hemodynamics with mechanobiology in patient-specific computational models of ATAAs

correspondence: *Stéphane Avril, Mines Saint-Étienne, Univ Lyon, Univ Jean Monnet, INSERM, U1059 Sainbiose, F - 42023 Saint-Étienne France.
Phone: 0477420188, Fax: +33477420000, e-mail: avril@emse.fr

[†]These authors have equally contributed to this work as first authors.

Abstract

Background and Objective. The prevention of ascending thoracic aortic aneurysms (ATAAs), which affect thousands of persons every year worldwide, remains a major issue. ATAAs may be caused by anything that weakens the aortic wall. Altered hemodynamics, which concerns a majority of patients with bicuspid aortic valves, has been shown to be related to such weakening and to contribute to ATAA development and progression. However the underlying mechanisms remain unclear and computational modeling in this field could help significantly to elucidate how hemodynamics and mechanobiology interact in ATAAs.

Methods. Accordingly, we propose a numerical framework combining computational fluid dynamics and 4D flow magnetic resonance imaging (MRI) coupled with finite element (FE) analyses to simulate growth and remodeling (G&R) occurring in patient-specific aortas in relation with altered hemodynamics. The geometries and the blood velocities obtained from 4D flow MRI are used as boundary conditions for CFD simulations. CFD simulations provide an estimation of the wall shear stress (WSS) and relative residence time (RRT) distribution across the luminal surface of the wall. An initial insult is then applied to the FE model of the aortic wall, assuming that the magnitude of the insult correlates spatially with the normalized RRT distribution obtained from CFD simulations. G&R simulations are then performed. The material behavior of each Gauss point in these FE models is evolved continuously to compensate for the deviation of the actual wall stress distribution from the homeostatic state after the initial insult. The whole approach is illustrated on two healthy and two diseased subjects. The G&R parameters are calibrated against previously established statistical models of ATAA growth rates.

Results. Among the variety of results provided by G&R simulations, the analysis focused especially on the evolution of the wall stiffness, which was shown to be a major risk factor for ATAAs. It was shown that the G&R parameters, such as for instance the rate of collagen production or cell mechanosensitivity, play a critical role in ATAA progression and remodeling.

Conclusions. These preliminary findings show that patient-specific computational modeling coupling hemodynamics with mechanobiology is a promising approach to explore aneurysm progression.

keywords: Ascending Thoracic Aortic Aneurysm; Mechanobiology; Computational Fluid Dynamics; Growth and remodeling; Constrained mixture theory.

Introduction

The human thoracic aorta has a complex morphology which is susceptible to localized ballooning, especially between the root and the arch, where it is referred to as aneurysm. When they are not congenital, Ascending thoracic aortic aneurysms (ATAAs) occur mostly in the aged individuals [1]. Thoracic aortic aneurysms have an estimated incidence of at least 6-10 per 100,000 person-year [2]. Aortic dissection is the most devastating complication of ATAAs. It is a life-threatening condition associated with very high morbidity and mortality rates, and it remains a challenge to anticipate and treat. ATAAs may be caused by anything that weakens the aortic wall and understanding the weakening process is essential for preventing type A dissections. In this work, we focus on the role of altered hemodynamics, which concerns a majority of patients with bicuspid aortic valves, but also a fraction of patients with tricuspid aortic valves [3], and which has been shown to contribute significantly to ATAA development and progression, although it is often combined with other biomechanical factors [4].

The critical role of hemodynamics in arterial development, adaptation, and in vascular physiopathology has been investigated for decades [5]. Hemodynamics parameters cannot be directly related to the risk of rupture of aneurysms [6] but their action on the endothelium, through the wall shear stress (WSS), can trigger a number of pathways participating in weakening the aortic wall through different adaptation processes and microstructural changes [7]. Nevertheless, the mechanisms by which the WSS distribution affects the progression of ATAAs and inter-

acts with complex intramural biochemical and biomechanical processes remain poorly understood.

Low WSS is known to induce atherosclerosis [8] whereas high relative residence time (RRT) levels, found near post-stenotic regions, are associated with endothelial dysfunctions [9]. However, many effects are intertwined in ATAAs due to complex flow patterns. Nowadays, these flow patterns can be well captured using 4D flow Magnetic Resonance Imaging (MRI). Important morphological, structural and biomechanical modifications occur concomitantly to hemodynamics alterations during the progression of ATAAs. However, beyond inferring links between hemodynamics and mechanobiology, there is a pressing need to elucidate how hemodynamics and mechanobiology interact in ATAA progression. For that, establishing computational models coupling hemodynamics and mechanobiology appears as a very promising approach [10]. Although many computational models of aneurysm evolution disregarded the interactions with the blood flow, a fraction of them attempted to couple WSS with the growth and remodeling (G&R) equations of arteries [11–17].

No attempt has ever been achieved for ATAAs where the precise role of WSS remains controversial. Using 4D flow MRI and post-operative histological analyses, Guzzardi et al. [18] found that regions with large WSS (often located where a jet flow coming from the left ventricle inpinges the wall of the ascending aorta) undergo greater elastin degradation associated with vessel wall remodeling, whereas adjacent regions with normal WSS have less elastin degradation. They concluded that regions of high WSS in ATAAs correspond to regions of extracellular matrix

(ECM) dysregulation and elastic fiber degeneration. This was specific to BAV patients though, pointing to valve-related hemodynamics as a contributing factor in the development of aortopathy.

This indicates that supplemental efforts in terms of computational modeling are still required to gain insight into the adaptive G&R effects occurring in ATAAs. Consequently, the objective of the present work is to establish a computational framework coupling patient-specific hemodynamics of ATAAs [19, 20] with a computational G&R model which was previously adapted for human ATAAs [21]. After presenting the comprehensive framework, we illustrate the whole approach on two healthy and two diseased subjects on whom we assume a direct relationship between certain hemodynamics metrics, such as WSS or RRT, and the original insult causing microstructural changes in the aortic wall, and predict the induced G&R effects across the ascending thoracic aorta.

Materials and methods

Study population

In this work, we introduce a numerical framework combining patient-specific computational fluid dynamics (CFD) and structural Finite Element Analyses (FEA) to simulate G&R in ATAAs. The approach is illustrated on two healthy and two diseased subjects. The protocol was approved by the Institutional Review Board of the University Hospital Center of Saint-Etienne and informed consent was obtained from the participants. 4D flow MRI datasets were acquired and employed

to reconstruct the geometry of their aorta and to assess their blood flow velocities. The subjects' characteristics are reported in Table 1.

Computational fluid dynamics (CFD)

4D flow MRI acquisition and pre-processing

4D flow MRI datasets were acquired using a Siemens Magnetom Prisma 3T MR scanner. In 4D flow MRI, velocity is encoded along the three spatial dimensions throughout the cardiac cycle, thus providing a dynamic imaging of 3D velocity fields. The velocity encoding is based on the changes in the phase of the magnetic resonance (MR) signal along a magnetic field gradient and is directly related to the blood flow velocity. A 4D flow dataset consists of the 3 components of local velocity vectors (V_x, V_y & V_z) throughout the cardiac cycle. 4D MRI data acquisition relies on efficient synchronization between cardiac and respiratory movements leading to optimized scan times of about 20 minutes [22]. The main parameters of ECG gating and 4D MRI data acquisition were: spatial resolution = 2.4 $\times$ 2.4 $\times$ 2.4 mm^3, field of view (FOV) = 380 $\times$ 285 mm^2, velocity encoding (VENC) = 200 cm/s, Bandwidth (BW) = 496 Hz/Pixel, Flip angle = 7^o, echo time (TE) / repetition time (TR) = 2.19 / 37.9 and phase duration = 37.9 ms. 4D flow MRI datasets were pre-processed using the velocity Mapping Tool (Tool for preprocessing & converting of 4D flow MRI data- Freiburg University, Germany & Northwestern University, USA) developed in MATLAB (MathWorks Inc. R2015b). The correction strategies employed were eddy current correction,

noise filtering, anti-aliasing. The corrected data were exported to Ensight, CEI, Inc., a 3D blood flow visualization software. The local flow velocity maps could then be obtained at any cross section. In order to quantify local WSS distributions in complex flows, a computational framework combining 4D flow MRI with CFD was developed [19]. The pre-processed dicom images were used for the 3D reconstruction of the aortic geometry needed to define the CFD domain, based on the center-line method and using splines to fit the contours [19]. The reconstructed geometry included the ascending thoracic aorta, the aortic arch with the apico-aortic branches and the descending thoracic aorta. It was then exported to Ansys-Fluent (ANSYS, Academic research, Release 17.2) where it was meshed with tetrahedral elements before performing the CFD simulations. The number of tetrahedra used in the present study is reported in Table 2. A mesh sensitivity analysis was conducted, it showed that increasing the number of tetrahedra by a factor 2 induced relative variations of the obtained pressure and velocity fields which were less than 2%.

Boundary conditions and solver setup parameters

The velocity distribution obtained from 4D flow MRI were applied as boundary conditions in the CFD models at the ascending aorta inlet and apico-aortic branches. Pressure boundary conditions were also applied at the outlet of the descending thoracic aorta wherein a three-element Windkessel model was employed to represent the physiological blood pressure. The incompressible Navier-Stokes equations were solved, assuming the blood flow as laminar, non-Newtonian and

incompressible with a density of 1050 kg/m^3. The non-Newtonian behavior was represented using the Carreau-Yasuda model

$$\mu = \mu_\infty + (\mu_0 - \mu_\infty)[1 + (\lambda\dot{\gamma})^\alpha]^{\frac{n-1}{\alpha}} \tag{1}$$

where $\dot{\gamma}$ represents the scalar shear rate, μ_0=0.042 Pa.s is the blood viscosity at low shear rate, μ_∞=0.00345 Pa.s is the blood viscosity at high shear rate, λ = 3.31s is a time constant, n=0.375 is the power law index and α=2 is the Yasuda exponent [23].

The aortic walls were assumed to be rigid, impermeable and with a no-slip condition (*i.e.* velocity on the wall is zero). The resolution was achieved with Ansys Fluent v17.2 using the Semi-Implicit Method for Pressure-Linked Equations (SIMPLE), a second-order interpolation scheme and a second-order upwind interpolation. A transient-time solver was used, with a second order implicit integration time and a time step of 1 ms. The threshold for residual errors was set to 10^{-3}. To reach fully developed flows and to avoid unsteady state solution due to initial transient conditions, the simulation was performed for three cardiac cycles and the last cycle only was used for post processing.

Hemodynamics descriptors

The RRT hemodynamics descriptor was computed according to the following formula [9, 24]:

$$\text{RRT} = \frac{1}{(1 - 2 \times \text{OSI}) \times \text{TAWSS}} \tag{2}$$

where

$$\text{TAWSS} = \frac{1}{T}\int_0^T |\text{WSS}|\, dt \tag{3}$$

$$\text{OSI} = 0.5\left(1 - \frac{\left|\int_0^T \text{WSS} dt\right|}{\int_0^T |\text{WSS}|\, dt}\right) \tag{4}$$

T is the period of the cardiac cycle and WSS is the instantaneous wall shear stress: WSS$= \mu\frac{\partial v}{\partial n}$, where $\frac{\partial v}{\partial n}$ is the normal velocity gradient (shear rate) and μ is the dynamic viscosity of the fluid.

Statistical model of ATAA progression

The aortic diameters of the four subjects enrolled in this study are reported in Table 1. We used a statistical model to calibrate the G&R parameters driving the temporal evolution of the aortic diameter during ATAA progression, taking into account sex (S), age (A) and body surface area (BSA). These factors are known to play a major role in the progression of aortic diameter [7, 25–28] especially in ATAA patients. The evolution of aortic diameter follows an exponential function with time [25], which may be written:

$$\text{AD} = \text{A} \times exp(\text{BSA} \times \text{S} \times t) + \text{ID}, \tag{5}$$

where AD, A, BSA, S, t, ID represent respectively: the aortic diameter, age (A takes the value 0.008 for age ≤ 55 and 0.01 for age ≥ 55), body surface area index, sex (S takes the value 0.15 for male and 0.24 for female), time after the first MRI

examination in years and diameter of the ascending aorta at the first examination. These parameters are fixed based on the assumption that the aneurysm growth rate for females is 1.19 $\pm$ 1.15 mm per year and 0.59 $\pm$ 0.66 mm per year for males [28] . The BSA was calculated based on the Dubois & Dubois [29] formula which may be written such as:

$$\mathrm{BSA} = \mathrm{W}^{0.425} \times \mathrm{H}^{0.725} \times 0.20247, \tag{6}$$

where W and H represents the weight in 'kg' and height in 'm' of the subject (Table 1).

Finite–Element model of G&R

The patient-specific geometry of each subject's aorta was reconstructed using 4D flow MRI scans at diastole, which were processed by an in-house code. A structural mesh composed of shell elements was reconstructed based on the centerline obtained by VMTK [30]. Whereas the fluid domain was modeled with tetrahedra for CFD analyses, a 3D structural mesh made of hexahedral elements was reconstructed to simulate G&R using FEA. The mesh was obtained by applying a patient-specific homogeneous thickness across the arterial wall on the shell elements. The mesh was structural, which means that the edge of each element was locally aligned with the material directions of the artery: radial, circumferential and axial. The radial direction was defined as the outward normal direction to the luminal surface, the axial direction was defined as the direction parallel to

the luminal centerline and the circumferential direction was perpendicular to the two previously defined directions. The G&R model was implemented within the commercial FE software Abaqus [31] through a coupled user material subroutine (UMAT) [21]. More details about this material model are given in Appendix B. As boundary conditions, a uniform pressure of 100 mmHg was applied on the luminal surface. It was found in a previous study [32] that pressure variations are less than 5% across the surface of the ascending aorta. Moreover, at the inlet and outlet boundaries of the G&R model, only radial displacements were allowed, but circumferential and axial displacements were fixed.

The deformation of the artery was computed at every time-step (1 month) for a duration of 10 years. The nonlinear equations resulting from equilibrium satisfaction at every time-step were solved using the Newton Raphson method. G&R deformations tensors at each time step were derived based on stresses assessed at the previous step. It was assumed that homeostatic conditions were satisfied at the first step.

Sensitivity analyses

Our computational model was designed to predict the G&R response of a thick-wall patient-specific ATAA model after an initial insult. For the latter we considered a localized elastin loss driven by the local normalized RRT defined such as:

$$\zeta_{\mathrm{RRT}} = \mathrm{RRT}/\mathrm{RRT}_{\mathrm{max}}. \tag{7}$$

As the RRT distribution was only needed to apply the initial insult of the G&R model, it was not necessary to perform CFD analyses iteratively during ATAA progression. Only the first CFD analysis was needed.

ATAA progression was calibrated to follow the same diameter change as the one given by the statistical model of Eq. 5. For that, we adjusted the gain parameters of collagen k_σ^i of the material model defined in Appendix.

It was also suggested that many patients developing ATAAs may also suffer from an impairment of smooth muscle cell (SMC) mechanosensitivity [33]. In order to take into account a possible combination of factors (elastin degradation, mechanosensitivity impairment), we introduced a factor standing for the mechanosensitivity impairment factor, such that the target homeostatic stress would be erroneously targeted by SMCs as $1.05\sigma_h$ or $1.1\sigma_h$ instead of σ_h when there is a mechanosensitivity impairment (Equation 13 in Appendix B).

Results

Results obtained on four subjects with our novel integrated computational framework are now presented in this section, focusing at the following variables: WSS, RRT, temporal progression of maximum aortic diameter and local tangent stiffness. The streamlines of blood velocity computed at peak systole for each subject are shown in the supplemental materials (Fig. S3).

Wall Shear Stress (WSS)

The WSS contours for the two healthy and two diseased subjects at peak systole are shown in Fig. 2 and Fig. 3.

For the two subjects harboring an ATAA, the WSS magnitude is lower in the ascending thoracic aorta compared to other regions of the aorta (Fig. 3). The mean WSS is 1.7 Pa for Aneurysmal 1 and 0.5 Pa for Aneurysmal 2 (Fig. 4).

For the two healthy subjects, WSS contours (Fig. 2) are rather uniform along the length of the aorta. The mean WSS in the ascending thoracic aorta is 3.3 Pa (Fig. 4), which is higher than in the diseased patient.

Relative Residence Time (RRT)

Figures 5 and 6 show RRT contours obtained for the four subjects. For the two healthy patients, RRT in the ascending thoracic aorta is lower than in other regions of the aorta (Fig. 5). The mean RRT is 5 (Fig. 7), which is lower than in the ATAA patients. The RRT distribution in both diseased patients shows some blood stagnation in the ascending thoracic aorta. The mean RRT for Aneurysmal 1 is 8 and for Aneurysmal 2 is 17 (Fig. 7).

G&R effects

Elastin degradation scaled by the local normalized RRT is responsible for non homeostatic stresses in the ascending thoracic aorta. In response to this deviation from homeostasis, G&R leads to an increase of the aortic diameter in the whole

ascending thoracic aorta. The parameter of collagen deposition is adjusted in order to obtain diameter progressions in agreement with the statistical model of Eq. 5, as shown in Fig. 8. The obtained parameters are 0.04 for healthy subjects and 0.7 for diseased subjects. With these parameters, both healthy and aneurysm subjects showed aortic enlargement. Then, among the variety of results provided by such G&R simulations, the analysis focused especially on the evolution of the wall stiffness, which was shown to be a major risk factor for ATAAs [34–36]. The local stiffness of the aortic wall was derived from the model according to

$$E_\theta = \frac{\sigma_\theta^{\text{sys}} - \sigma_\theta^{\text{dia}}}{\epsilon_\theta^{\text{sys}} - \epsilon_\theta^{\text{dia}}} \tag{8}$$

where σ_θ and ϵ_θ stand for stresses and strains in circumferential directions, respectively, and superscripts "dia" and "sys" indicates diastolic and systolic instances, respectively. Note that we focus here on the circumferential stiffness as it can be derived from circumferential strains induced by pressure variations at every heart beat and thus it can have a clinical interest [34, 36].

Figs. 9 and 10 show the obtained stiffness after 10 years in healthy and diseased patients, respectively, when the factor for mechanosensitivity impairment is set to 1, 1.05 or 1.1 (corresponding to homeostatic stresses of σ_h, $1.05\sigma_h$ and $1.1\sigma_h$ respectively). The results show that mechanosensitivity impairment induces larger stiffness values but does not affect significantly diameter changes (Tables 4 and 5). Indeed, if there is a mechanosensitivity impairment, the new collagen fibers are deposited with a higher tension. As collagen fibers have an exponential

stress-strain response, a higher tension means a higher stiffness. This explains why the mechanosensitivity impairment induces a higher stiffness. But the impairment does not affect the progression rate of the aneurysm, which is mostly governed by the gain parameters of Eq. 13 (see Appendix B).

Discussion

Altered hemodynamics in patients harboring an ATAA is known to affect endothelial cells. However, it remains unclear how this can participate in ATAA progression, which is controlled by the intramural cells (SMCs, fibroblasts) and ECM. Therefore, our new computational modeling framework, coupling hemodynamics and vessel wall adaption, can be helpful to elucidate how hemodynamics and mechanobiology interact in ATAAs and bring insight into the disease progression. Solving the coupled fluid-solid-growth problem numerically in patient-specific geometry implies high computational costs. In order to overcome these computational challenges and reach accurate predictions, our novel computational framework combines 4D flow MRI and CFD to evaluate the hemodynamics descriptors. Coupling our recent G&R models [21] with the predicted hemodynamics [19, 20], we showed that factors such as RRT, by its potential relationship with ECM degeneration [37], may trigger aortic stiffening and ATAA progression, and that possible mechanosensitivity impairment of SMCs can accelerate the stiffening effects, which were shown to increase the risk of rupture [34–36].

The G&R model took into account various structurally substantial constituents,

namely elastin, collagen fiber families and SMCs, allowing them to undergo turnover within the framework of the constrained mixture theory (CMT) [21, 38, 39]. Turnover rates of collagen fibers and SMCs were stress mediated and proportional to a deposition rate. We assumed that stimuli for tissue adaptation and maintenance were always triggered by RRT levels. Other factors related to hemodynamics forces could also be considered as potential triggers of a G&R response. Peak WSS values are usually invoked [18]. Our CFD simulations showed that WSS distribution in diseased patients varies between the location in the dilated region and along the aortic length. But the WSS remained between 1 and 7 Pa, and for these values, the aorta would usually be considered as healthy and devoid of any damage [40].

Low WSS or large RRT is known to enhance the attachment of platelets and thrombogenic proteins to the arterial walls, which may induce disease progression [41]. Our CFD simulations show that low WSS was found in the ascending thoracic aorta and exacerbated for both diseased patients. Low WSS in the aortic walls may induce endothelial dysfunction, causing wall thickening and possible ATAA progression [40]. Studies show that high WSS ($i.e \geq 7$) may cause endothelial damage and promote plaque rupture but this is not yet very clear [42].

In our analyses, the WSS and RRT distributions were used to create the insult (local elastin degradation) that induces the subsequent aneurysm growth. This insult occurs at the beginning of the analyses and causes adaptations of the aorta for 10 years. In future work, we could also consider successive insults over these 10 years. This would require to redo the CFD simulations with the updated geometry.

Salient trends of arterial adaptation to altered hemodynamics were previously captured by 2D and 3D thin walled or membrane and representative straight cylindrical artery based on CMT models [43, 44]. Despite the major progress these prior studies on CMT-based models have permitted, two further improvements can be emphasized in the current work: application of CMT-based models to patient-specific geometries and integration of layer-specific properties (media and adventitia). Fluid-solid-growth simulations were developed for cerebral [45] or abdominal [46–49] aneurysms. The current work initiates G&R simulations where one important metric is derived from an initial CFD simulation (one-time and one-way coupling).

RRT was previously found to be a useful parameter for identifying atheroprone regions [50, 51]. Our model, by design, suggests that RRT plays an important role in disease progression. In future studies, the model could be used in a reverse engineering analysis to find intrinsic relationships between patient-specific RRT distributions and long-term aneurysm progression measured in human patients. This could contribute to investigate more thoroughly the role of RRT in ATAA progression.

Limitations of our approach are related to the clinical validation, which should be based on patients followed longitudinally over a sufficiently long period and with appropriate imaging modalities (including 4D MRI at the initial time point). In the meantime, the model can be validated against data on animal models, as already performed several times for CMT-based models [52]. Limitations are also related to the rigid wall assumption of the CFD model. The rigid wall assumption

enables significant reductions of computational times compared to fluid structure interaction (FSI) simulations achieved in the thoracic aorta [32]. The computational time was decisive to enable running all the simulations presented in the current study. However, neglecting the motion of the aortic walls can induce errors in the temporal variations of the blood flows. For that reason, we usually focus on time-integrated quantities (RRT for instance) instead of instantaneous quantities. In previous studies, we found that the impact of the rigid wall assumption on the maximum WSS values at systole was not significant, which convinced us to report WSS as well. This is very specific to large arteries, for which the assumption of rigid and impermeable walls was already shown to be reasonable for WSS predictions [53]. Another limitation is that the same pressure is maintained constant throughout the 10 years of the G&R simulated process. Pressure evolutions would actually occur but these evolutions need to be measured, they cannot be predicted with the computational model. It is also worth mentioning that we had to resort to a statistical model to relate the ATAA progression rates to the sex, age and body surface area of aneurysmal patients. There is currently no mechanistic model that can easily relate the gain parameters of the G&R model (which govern ATAA progression rates) to clinical markers of a patient.

In summary of this work, hemodynamics and mechanobiology effects in ATAAs were coupled through a CFD model evaluating hemodynamics factors in ATAAs and using then to simulate G&R effects with FEA. We illustrated the potential of this novel computational approach to evaluate thoroughly the assumption that localized elastin loss in the ascending thoracic aorta at locations of large RRT fac-

tors in disturbed blood hemodynamics can trigger ATAA progression and aortic stiffening. It was shown that the rate of collagen production or cell mechanosensitivity may play a critical role in ATAA progression and aortic stiffening. These preliminary findings show that patient-specific computational modeling coupling hemodynamics with mechanobiology is a promising approach to explore ATAA initiation and progression. Future work will focus on model predictability at a patient-specific level by following up a cohort of ATAA patients over a significant number of years.

Acknowledgements

The authors are grateful to the European Research Council for grant ERC-2014-CoG BIOLOCHANICS, grant number 647067. The authors also thank Siemens Healthineers for their technical support and more specifically Ning Jin, Andreas Greiser and Sinyeob Ahn for making available the 4D flow 785A prototype sequence. We are also grateful to Ansys, Inc. for providing Ansys-Fluent (ANSYS® Academic Research, Release 17.2).

Conflict of interest

The authors have no conflict of interest to declare concerning the contents of this manuscript.

References

[1] Ali N Azadani, Sam Chitsaz, Alex Mannion, Aart Mookhoek, Andrew Wisneski, Julius M Guccione, Michael D Hope, Liang Ge, and Elaine E Tseng. Biomechanical properties of human ascending thoracic aortic aneurysms. *The Annals of Thoracic Surgery*, 96(1):50–58, 2013.

[2] G. A. Kuzmik, A. X. Sang, and J. A. Elefteriades. Natural history of thoracic aortic aneurysms. *Journal of Vascular Surgery*, 56:565–71, 2012.

[3] Raja Jayendiran, Salvatore Campisi, Magalie Viallon, Pierre Croisille, and Stéphane Avril. Hemodynamics alteration in patient-specific dilated ascending thoracic aortas with tricuspid and bicuspid aortic valves. *Journal of Biomechanics*, page 109954, 2020.

[4] Sarah Geisbüsch, Angelina Stefanovic, Deborah Schray, Irina Oyfe, Hung-Mo Lin, Gabriele Di Luozzo, and Randall B Griepp. A prospective study of growth and rupture risk of small-to-moderate size ascending aortic aneurysms. *The Journal of thoracic and cardiovascular surgery*, 147(1):68–74, 2014.

[5] A.C. Burton. Relation of structure to function of the tissues of the wall of blood vessels. *Physiol. Rev.*, 34:619–42, 1954.

[6] Tim McGloughlin. *Biomechanics and mechanobiology of aneurysms*. Springer, Heidelberg, 2011.

[7] Alban Redheuil, Wen-Chung Yu, Elie Mousseaux, Ahmed A Harouni, Nadjia Kachenoura, Colin O Wu, David Bluemke, and Joao AC Lima. Age-related changes in aortic arch geometry: relationship with proximal aortic function and left ventricular mass and remodeling. *Journal of the American College of Cardiology*, 58(12):1262–1270, 2011.

[8] Jing Zhou, Yi-Shuan Li, and Shu Chien. Shear stress–initiated signaling and its regulation of endothelial function. *Arteriosclerosis, thrombosis, and vascular biology*, 34(10):2191–2198, 2014.

[9] Konstantinos P Papadopoulos, Manolis Gavaises, Ioannis Pantos, Demosthenes G Katritsis, and Nicholas Mitroglou. Derivation of flow related risk indices for stenosed left anterior descending coronary arteries with the use of computer simulations. *Medical engineering & physics*, 38(9):929–939, 2016.

[10] Jay D Humphrey. Vascular mechanics, mechanobiology, and remodeling. *Journal of mechanics in medicine and biology*, 9(02):243–257, 2009.

[11] S. Baek, K.R. Rajagopal, and J.D. Humphrey. A theoretical model of enlarging intracranial fusiform aneurysms. *J Biomech Eng*, 128(1):142–9, 2006.

[12] S. Baek, A. Valentín, and J.D. Humphrey. Biochemomechanics of cerebral vasospasm and its resolution: II. constitutive relations and model simulations. *Ann Biomed Eng.*, 35:1498–509, 2007.

[13] A. Valentín, L. Cardamone, S. Baek, and J.D. Humphrey. Complementary vasoactivity and matrix remodelling in arterial adaptations to altered flow and pressure. *J R Soc Interface*, 6(32):293–306, 2009.

[14] Yixiang Feng, Shigeo Wada, Ken-Ichi Tsubota, and Takami Yamaguchi. Growth of intracranial aneurysms arised from curved vessels under the influence of elevated wall shear stress a computer simulation study. *JSME International Journal Series C Mechanical Systems, Machine Elements and Manufacturing*, 47(4):1035–1042, 2004.

[15] S. Kondo, N. Hashoimotot, H. Kikuchi, F. Hazama, I. Nagata, and H. Kataoka. Cerebral aneurysms arising at nonbranching sites. an experimental study. *Stroke*, 28:398–404, 1997.

[16] S. Ahn, D.Shin, S. Tateshima, K. Tanishita, F. Vinuela, and S. Sinha. Fluid-induced wss in anthropomorphic brain aneurysm models: MR phase-contrast study at 3T. *J Magn Reson Imaging*, 25:1120–30, 2007.

[17] Y. Hoi, H. Meng, S.H. Woodward, B.R. Bendok, R.A. Hamel, L.R. Guterman, and L.N. Hopkins. Effects of arterial geometry on aneurysm growth: Three dimensional computational fluid dynamics study. *J Neurosurg*, 101:676–81, 2004.

[18] D.G. Guzzardi, A.J. Barker, P. van Ooij, S.C. Malaisrie, J.J. Puthumana, D.D. Belke, H.E. Mewhort, D.A. Svystonyuk, S. Kang, S. Verma, J. Collins, J. Carr, R.O. Bonow, M. Markl, J.D. Thomas, P.M. McCarthy, and P.W.

Fedak. Valve-related hemodynamics mediate human bicuspid aortopathy: Insights from wall shear stress mapping. *J Am Coll Cardiol*, 66(8):892–900, 2015.

[19] F. Condemi, S. Campisi, M. Viallon, T. Troalen, G. Xuexin, A. J. Barker, M. Markl, P. Croisille, O. Trabelsi, C. Cavinato, A. Duprey, and S. Avril. Fluid and Biomechanical Analysis of Ascending Thoracic Aorta Aneurysm with Concomitant Aortic Insufficiency. *Annals of Biomedical Engineering*, 45:2921–2932, 2017.

[20] Raja Jayendiran, Salvatore Campisi, Magalie Viallon, Pierre Croisille, and Stéphane Avril. Hemodynamics alteration in patient-specific dilated ascending thoracic aortas with tricuspid and bicuspid aortic valves. *Journal of Biomechanics*, 110:109954, 2020.

[21] S.J. Mousavi, S. Farzaneh, and S. Avril. Patient-specific predictions of aneurysm growth and remodeling in the ascending thoracic aorta using the homogenized constrained mixture model. *Biomech Model Mechanobiol*, 2019.

[22] Zoran Stankovic, Bradley D Allen, Julio Garcia, Kelly B Jarvis, and Michael Markl. 4d flow imaging with mri. *Cardiovascular diagnosis and therapy*, 4(2):173, 2014.

[23] Mariana Simão, Jorge Ferreira, António C Tomás, José Fragata, and He-

lena Ramos. Aorta ascending aneurysm analysis using cfd models towards possible anomalies. *Fluids*, 2(2):31, 2017.

[24] Julio Garcia, Alex J Barker, Jeremy D Collins, James C Carr, and Michael Markl. Volumetric quantification of absolute local normalized helicity in patients with bicuspid aortic valve and aortic dilatation. *Magnetic Resonance in Medicine*, 78(2):689–701, 2017.

[25] Y. Hirose, S. Hamada, and M. Takamiya. Predicting the Growth of Aortic Aneurysms: A Comparison of Linear vs Exponential Models. *Angiology: The Journal of Vascular Diseases*, 46:413–419, 1995.

[26] Ruby C Lo, Bing Lu, Mark F Conrad, Mark F Fillinger, Robina Matyal, Allen D Hamdan, and Marc L Schermerhorn. Relative importance of aneurysm diameter and body size for predicting aaa rupture in men and women. *Journal of Vascular Surgery*, 57(1):287–288, 2013.

[27] Maude Gagné-Loranger, Éric Dumont, Pierre Voisine, Siamak Mohammadi, and François Dagenais. Natural history of 40–50 mm root/ascending aortic aneurysms in the current era of dedicated thoracic aortic clinics. *European Journal of Cardio-Thoracic Surgery*, 50(3):562–566, 2016.

[28] K. Cheung, M. Boodhwani, K. L. Chan, L. Beauchense, A. Dick, and T. Coutinho. Thoracic Aortic Aneurysm Growth: Role of Sex and Aneurysm Etiology. *Journal of the American Heart Association*, 6:e003792, 2017. DOI:10.1161/JAHA.116.003792.

[29] D. Du Bois and E. F. Du Bois. A formula to estimate the approximate surface area if height and weight be known. 1916. *Nutrition*, 5:303–11, 1989.

[30] L. Antiga and D.A. Steinman. Robust and objective decomposition and mapping of bifurcating vessels. *IEEE Trans Med Imaging*, 23(6):704–13, 2004.

[31] Hibbit, Karlson, and Sorensen. *Abaqus-Theory manual*, 6.11-3 edition, 2011.

[32] Rossella Campobasso, Francesca Condemi, Magalie Viallon, Pierre Croisille, Salvatore Campisi, and Stéphane Avril. Evaluation of peak wall stress in an ascending thoracic aortic aneurysm using fsi simulations: effects of aortic stiffness and peripheral resistance. *Cardiovascular Engineering and Technology*, 9(4):707–722, 2018.

[33] Jay D Humphrey, Dianna M Milewicz, George Tellides, and Martin A Schwartz. Dysfunctional mechanosensing in aneurysms. *Science*, 344(6183):477–479, 2014.

[34] Ambroise Duprey, Olfa Trabelsi, Marco Vola, Jean-Pierre Favre, and Stéphane Avril. Biaxial rupture properties of ascending thoracic aortic aneurysms. *Acta Biomaterialia*, 42:273–285, 2016.

[35] S. Farzaneh, O. Trabelsi, and S. Avril. Inverse identification of local stiffness across ascending thoracic aortic aneurysms. *Biomech Model Mechanobiol*, 10.1007/s10237-018-1073-0, 2018.

[36] S. Farzaneh, O. Trabelsi, B. Chavent, and S. Avril. Identifying local arterial stiffness to assess the risk of rupture of ascending thoracic aortic aneurysms. *Ann Biomed Eng*, 47(4):1038–50, 2019.

[37] Jean-Baptiste Michel, Guillaume Jondeau, and Dianna M Milewicz. From genetics to response to injury: vascular smooth muscle cells in aneurysms and dissections of the ascending aorta. *Cardiovascular research*, 114(4):578–589, 2018.

[38] S Jamaleddin Mousavi and Stéphane Avril. Patient-specific stress analyses in the ascending thoracic aorta using a finite-element implementation of the constrained mixture theory. *Biomechanics and modeling in mechanobiology*, 16(5):1765–1777, 2017.

[39] S.J. Mousavi, S. Farzaneh, and S. Avril. Computational predictions of damage propagation preceding dissection of ascending thoracic aortic aneurysms. *Int J Numer Method Biomed Eng*, 34(4):e2944, 2018.

[40] Håvard Nordgaard, Abigail Swillens, Dag Nordhaug, Idar Kirkeby-Garstad, Denis Van Loo, Nicola Vitale, Patrick Segers, Rune Haaverstad, and Lasse Lovstakken. Impact of competitive flow on wall shear stress in coronary surgery: computational fluid dynamics of a lima–lad model. *Cardiovascular Research*, 88(3):512–519, 2010.

[41] Xiao Liu, Anqiang Sun, Yubo Fan, and Xiaoyan Deng. Physiological signif-

icance of helical flow in the arterial system and its potential clinical applications. *Annals of biomedical engineering*, 43(1):3–15, 2015.

[42] Yusaku Fukumoto, Takafumi Hiro, Takashi Fujii, Genta Hashimoto, Tatsuhiro Fujimura, Jutaro Yamada, Takayuki Okamura, and Masunori Matsuzaki. Localized elevation of shear stress is related to coronary plaque rupture: a 3-dimensional intravascular ultrasound study with in-vivo color mapping of shear stress distribution. *Journal of the American College of Cardiology*, 51(6):645–650, 2008.

[43] I. Karšaj, J. Sorić, and J.D. Humphrey. A 3-d framework for arterial growth and remodeling in response to altered hemodynamics. *Int J Eng Sci*, 48(11):1357–72, 2010.

[44] J.D. Humphrey and K.R. Rajagopal. A constrained mixture model for growth and remodeling of soft tissues. *Math Models Methods Appl Sci*, 12(03):407–30, 2002.

[45] P.N. Watton, N.B. Raberger, G.A. Holzapfel, and Y. Ventikos. Coupling the hemodynamic environment to the evolution of cerebral aneurysms: computational framework and numerical examples. *J Biomech Eng*, 131(10):doi: 10.1115/1.3192141, 2009.

[46] A. Sheidaei, S.C. Hunley, S. Zeinali-Davarani, L.G. Raguin, and S. Baek. Simulation of abdominal aortic aneurysm growth with updating hemody-

namic loads using a realistic geometry. *Medical Engineering & Physics*, 33(1):80–88, 2011.

[47] A. Grytsan, P.N. Watton, and G.A. Holzapfel. Athick-walled fluid-solidgrowth model of abdominal aortic aneurysm evolution: application to a patient-specific geometry. *J Biomech Eng*, 137(3):031008, 2015.

[48] A.L. Marsden and J.A. Feinstein. Computational modeling and engineering in pediatric and congenital heart disease. *Current opinion in pediatrics*, 27(5):587, 2015.

[49] P. Di Achille, G. Tellides, and J.D. Humphrey. Hemodynamics-driven deposition of intraluminal thrombus in abdominal aortic aneurysms. *Int J Numer Method Biomed Eng*, 33(5):e2828, 2017.

[50] J. V. Soulis, O. P. Lampri, D. K. Fytanidis, and G. D. Giannoglou. Relative residence time and oscillatory shear index of non-newtonian flow models in aorta. In *2011 10th International Workshop on Biomedical Engineering*, pages 1–4, 2011.

[51] Demosthenes Katritsis, Lambros Kaiktsis, Andreas Chaniotis, John Pantos, Efstathios P Efstathopoulos, and Vasilios Marmarelis. Wall shear stress: theoretical considerations and methods of measurement. *Progress in cardiovascular diseases*, 49(5):307–329, 2007.

[52] Marcos Latorre and Jay D Humphrey. Modeling mechano-driven and

immuno-mediated aortic maladaptation in hypertension. *Biomechanics and Modeling in Mechanobiology*, 17(5):1497–1511, 2018.

[53] D. A. Steinman. *Assumptions in modelling of large artery hemodynamics*. Springer, Milano, 2012.

[54] F.A. Braeu, A. Seitz, R.C. Aydin, and C.J. Cyron. Homogenized constrained mixture models for anisotropic volumetric growth and remodeling. *Biomech Model Mechanobiol*, 16(3):889–906, 2017.

[55] Umberto Morbiducci, Raffaele Ponzini, Diego Gallo, Cristina Bignardi, and Giovanna Rizzo. Inflow boundary conditions for image-based computational hemodynamics: impact of idealized versus measured velocity profiles in the human aorta. *Journal of biomechanics*, 46(1):102–109, 2013.

[56] Pouya Youssefi, Alberto Gomez, Taigang He, Lisa Anderson, Nick Bunce, Rajan Sharma, C Alberto Figueroa, and Marjan Jahangiri. Patient-specific computational fluid dynamics—assessment of aortic hemodynamics in a spectrum of aortic valve pathologies. *The Journal of thoracic and cardiovascular surgery*, 153(1):8–20, 2017.

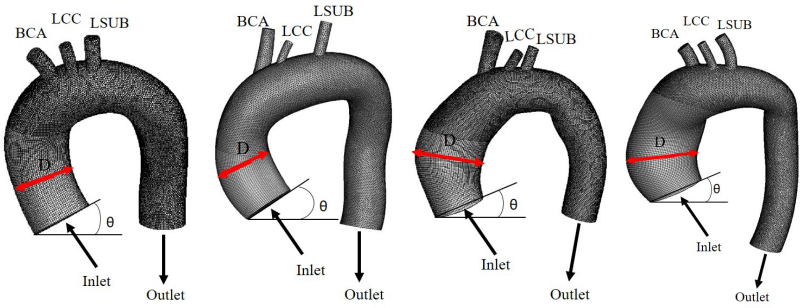

Figure 1: Finite-element meshes of the aortas for the four subjects a) Healthy 1 b) Healthy 2 c) Aneurysmal 1 and d) Aneurysmal 2 considered in this study, showing the inlet, outlet, branches, diameter and inlet angle

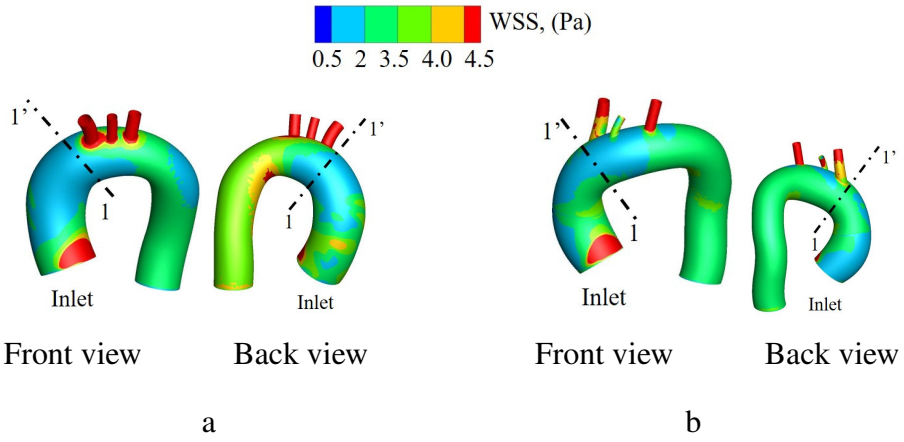

Figure 2: Wall shear stress patterns at peak systole obtained using CFD simulations for the two healthy subjects a) Healthy 1 and b) Healthy 2 considered in the current study. The cut-plane (1–1') shows the limit of what was considered as the ascending thoracic aorta in the analysis.

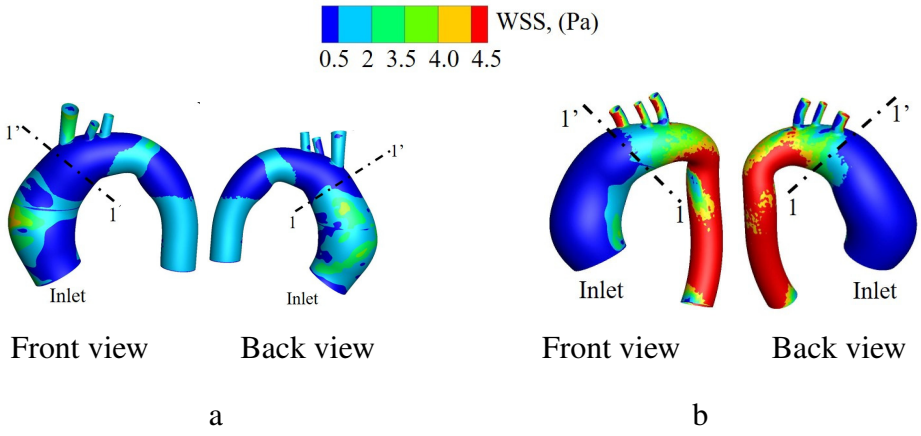

Figure 3: Wall shear stress patterns at peak systole obtained using CFD simulations for the two ATAA patients a) Aneurysmal 1 and b) Aneurysmal 2 considered in the current study. The cut-plane (1–1') shows the limit of what was considered as the ascending thoracic aorta in the analysis.

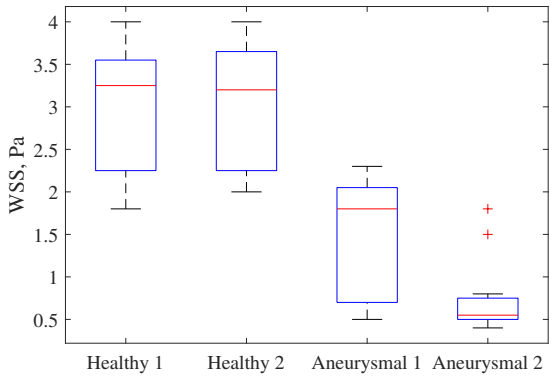

Figure 4: WSS distribution across the ascending thoracic aorta for the four subjects considered in this study. The central red line indicates the median, and the bottom and top edges of the boxes indicate the 25th and 75th percentiles, respectively. The outliers are shown using '+' symbol

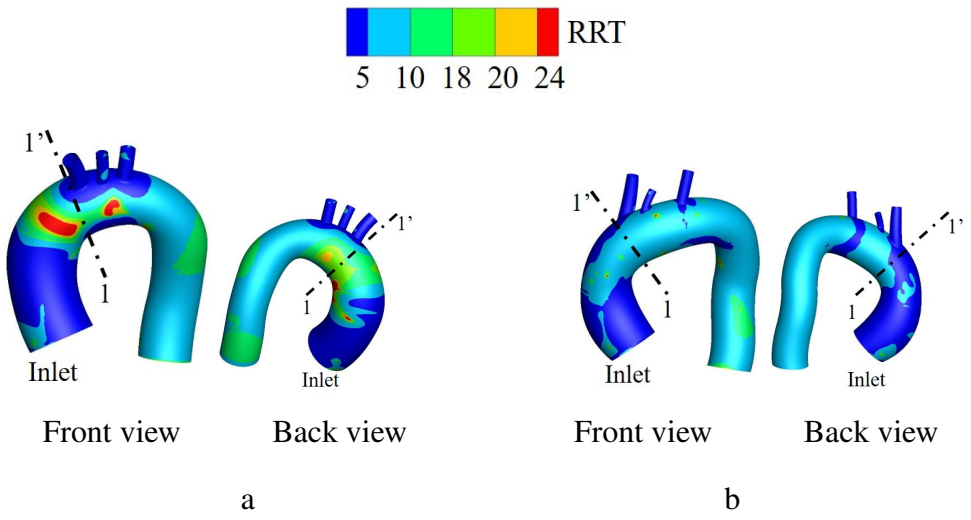

Figure 5: Relative Residence Time patterns obtained using CFD simulations for the two healthy subjects a) Healthy 1 and b) Healthy 2 considered in the current study. The cut-plane (1–1') shows the limit of what was considered as the ascending thoracic aorta in the analysis.

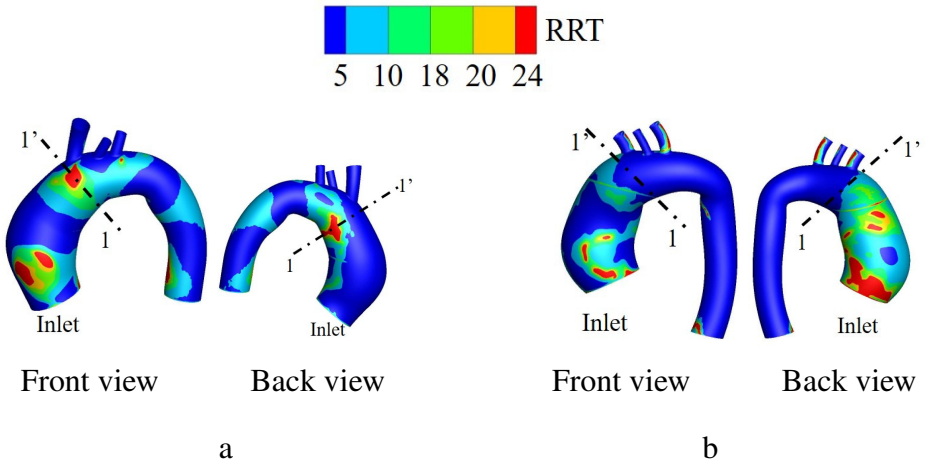

Figure 6: Relative Residence Time patterns obtained using CFD simulations for the two patients a) Aneurysmal 1 and b) Aneurysmal 2 considered in the current study. The cut-plane (1–1') shows the limit of what was considered as the ascending thoracic aorta in the analysis.

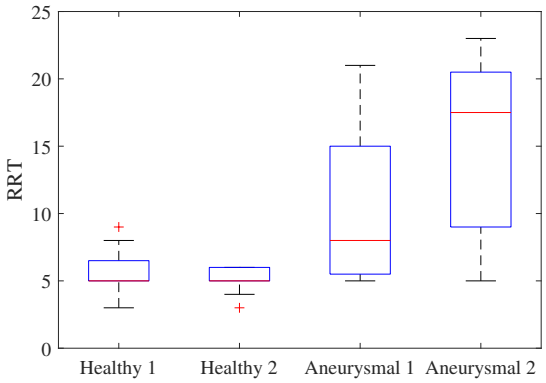

Figure 7: RRT distribution across the ascending thoracic aorta for the four subjects considered in this study. The central red line indicates the median, and the bottom and top edges of the box indicate the 25th and 75th percentiles, respectively. The outliers are shown using '+' symbol

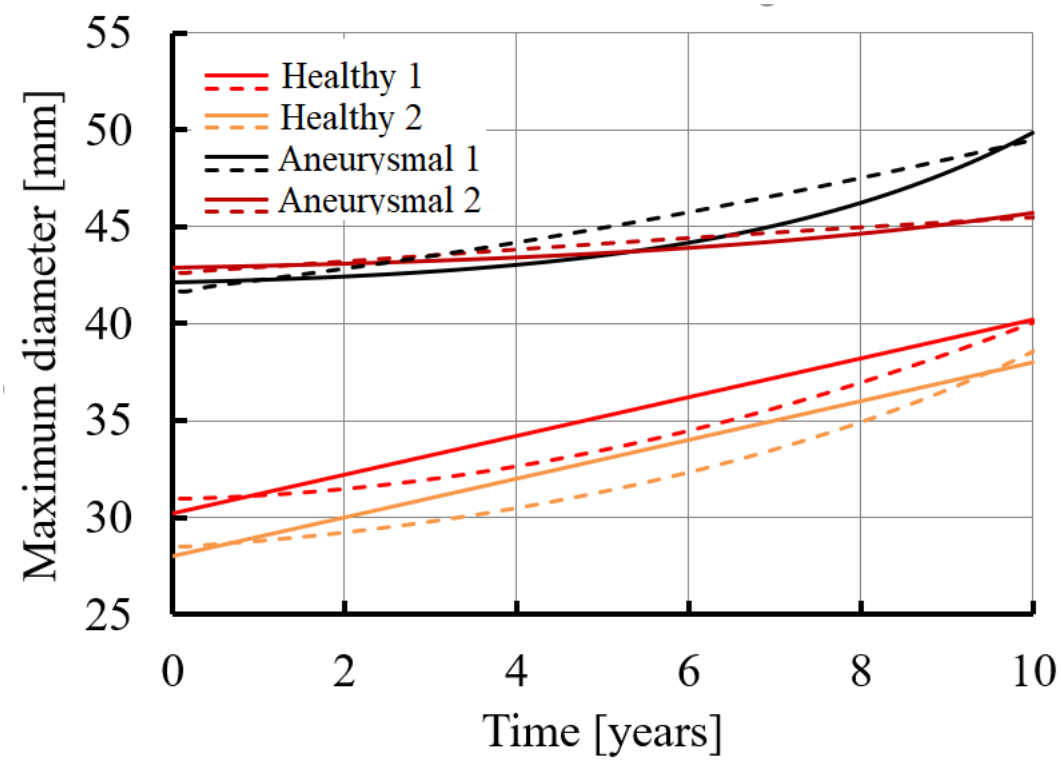

Figure 8: Temporal evolutions of the aortic maximum diameter obtained from our FEA simulations (dash lines) or predicted by the statistical model (solid lines) for the four subjects considered in this study: 2 healthy subjects (1 and 2) and 2 ATAA (3 and 4) patients.

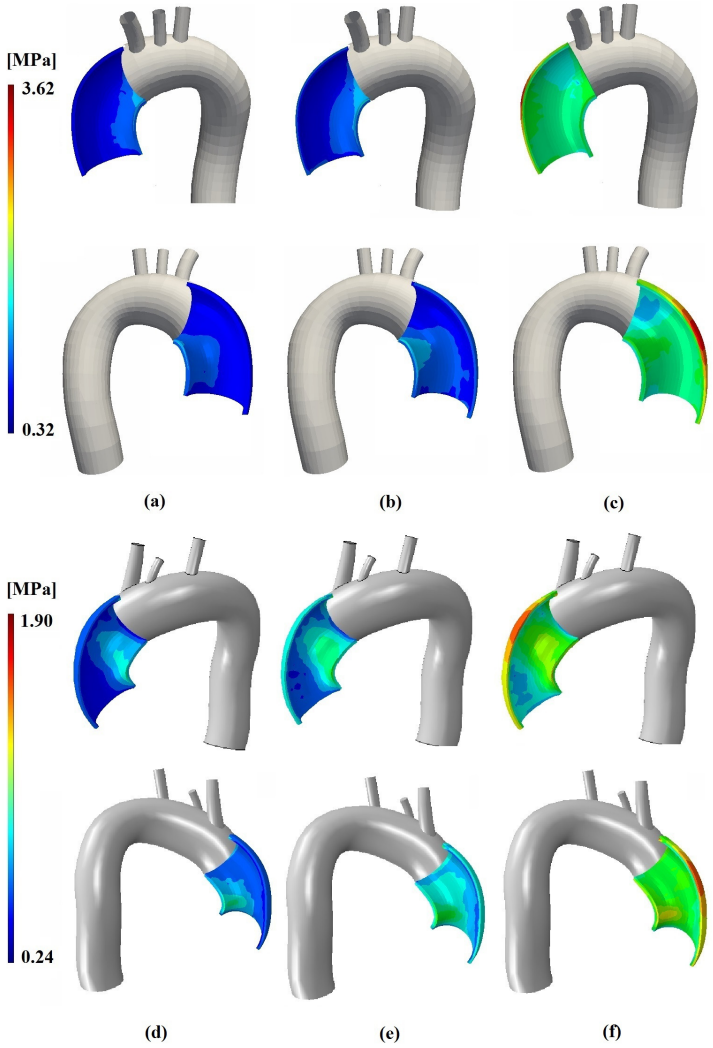

Figure 9: Distribution of the tangent aortic wall stiffness (structural stiffness) predicted by our simulation framework after 10 years of G&R in the first (a, b and c) and second (d, e and f) healthy subjects considered in this study, with 3 different conditions of mechanosensitivity impairment: a- and d- no mechanosensitivity impairment ($\sigma = \sigma_h$ at homeostasis), b- and e- mechanosensitivity impairment with $\sigma = 1.05\sigma_h$ at homeostasis) and c- and f- mechanosensitivity impairment with $\sigma = 1.1\sigma_h$ at homeostasis).

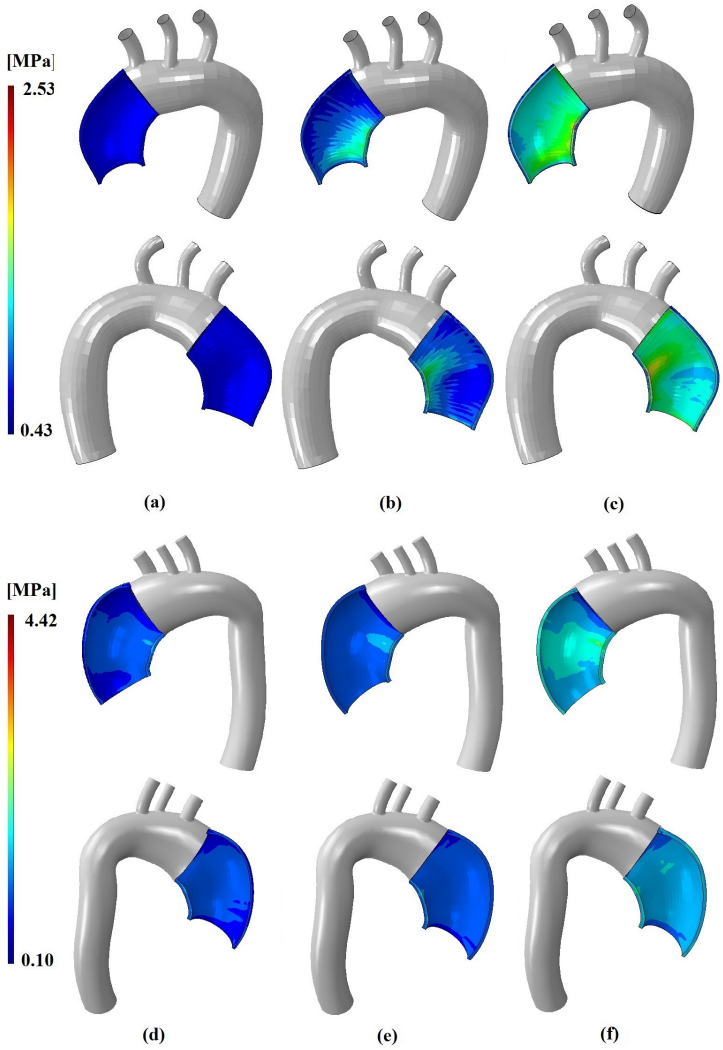

Figure 10: Distribution of the tangent aortic wall stiffness (structural stiffness) predicted by our simulation framework after 10 years of G&R in the first (a, b and c) and second (d, e and f) ATAA patients considered in this study, with 3 different conditions of mechanosensitivity impairment: a- and d- no mechanosensitivity impairment ($\sigma = \sigma_h$ at homeostasis), b- and e- mechanosensitivity impairment with $\sigma = 1.05\sigma_h$ at homeostasis) and c- and f- mechanosensitivity impairment with $\sigma = 1.1\sigma_h$ at homeostasis).

Table 1: Characteristics of the 2 healthy subjects and 2 ATAA patients considered in this study (TAV - Tricuspid Aortic valve; BAV- Bicuspid Aortic Valve).

Patient	Blood Pressure, mmHg	Age, Years	Sex	Weight, kg	Height, m	Ascending aorta diameter, mm	Valve phenotype
Healthy 1	110/80	69	Female	82	1.66	28.0	TAV
Healthy 2	110/80	51	Female	62	1.67	30.21	TAV
Aneurysmal 1	124/85	70	Female	64	1.58	42.13	TAV
Aneurysmal 2	130/100	50	Male	70	1.68	42.86	BAV

Table 2: Number of elements and nodes for the different meshes

	Fluid (CFD)		Solid (G&R)	
	Number of elements	Number of nodes	Number of elements	Number of nodes
Healthy 1	860,000	208,000	5,100	7,800
Healthy 2	661,000	193,000	5,300	8,100
Aneurysmal 1	952,000	268,000	4,500	6,900
Aneurysmal 2	1532,000	365,000	5,100	7,800

Table 3: Parameters employed for two–layer patient–specific human ATAA models adapted from [54]. α^{c_1}, α^{c_2}, α^{c_3} and α^{c_4} are axial, circumferential and two diagonal directions of collagen fiber families, respectively.

Symbol	**Values**
$\alpha^{c_j}, j = 1, 2, ..., 4$	0, $\frac{\pi}{2}$ and $\pm\frac{\pi}{4}$
μ^{e}	72 [J/kg]
κ	720 [J/kg]
$k_1^{\mathrm{c}_j}$	568 [J/kg]
$k_2^{\mathrm{c}_j}$	11.2
k_1^{m}	7.6 [J/kg]
k_2^{m}	11.4
ϱ_0^{e}	241.5 [kg/m^3]
$\varrho_0^{\mathrm{c}_1}$	65.1 [kg/m^3]
$\varrho_0^{\mathrm{c}_2}$	65.1 [kg/m^3]
$\varrho_0^{\mathrm{c}_3} = \varrho_0^{\mathrm{c}_4}$	260.4 [kg/m^3]
ϱ_0^{m}	157.5 [kg/m^3]
λ_z^{e}	1.25
λ^{c_j}	1.062
λ^{m}	1.1
T^{e}	101 [years]
T^{c_j}	101 [days]
T^{m}	101 [days]
t_{dam}	40 [days]
D_{max}	0.5
Thickness	1.8 [mm]

Table 4: Diameter (in mm) of the ascending thoracic aorta (at mid-length) after simulating 10 years of evolution

	σ=σ_h	σ=1.05σ_h	σ=1.1σ_h
Healthy 1	40.225	41.024	41.999
Healthy 2	39.782	38.936	39.536
Aneurysmal 1	49.56	50.39	50.795
Aneurysmal 2	45.49	46.134	46.723

Table 5: Average stiffness (in MPa) of the ascending thoracic aorta after simulating 10 years of evolution

	σ=σ_h	σ=1.05σ_h	σ=1.1σ_h
Healthy 1	0.504	0.66	2.349
Healthy 2	0.504	0.715	1.1
Aneurysmal 1	0.44	0.778	1.25
Aneurysmal 2	0.95	1.09	1.48

APPENDIX A: Computational Fluid Dynamics

Patient-specific boundary conditions

Patient-specific 4D flow MRI data were used to define the inflow velocity profile. Pixel-based time-varying velocities (V_x, V_y & V_z) were extracted from these 4D flow MRI data by using a in-house Matlab code (MathWorks Inc. R2015b) and mapped onto the inlet face of the aorta (Fig. S1). Therefore, every voxel of the inlet cross section was assigned a velocity vector varying both in space and time, whose direction and magnitude was determined from the 4D flow MRI data. The patient-specific pulsatile flow rate obtained from 4D flow MRI was set at the outlet cross sections of the apico-aortic branches (BCA, LCC, LSUB) (Fig. S1) [55, 56] as outflow boundary conditions. The measured flow rate waveforms from 4D flow MRI which are used as boundary conditions are shown in Fig. S2. A multiscale approach was implemented to describe the hemodynamics at the descending aorta outlet by coupling the 3D domain with a Three element Windkessel model. The three-element Windkessel model was tuned to represent the physiological blood pressure (Fig. S1). The three parameters, namely the peripheral resistance (resistor, R), the aortic compliance (capacitor, C) and the characteristic impedance (Z) were adjusted in such a way to match the physiological flow rate obtained from 4D flow MRI. Their values are reported in Table 6. The aortic walls were assumed to be rigid, impermeable and a no-slip condition was considered (*i.e.* Velocity on the wall is zero (v_{wall}=0)).

Table 6: Windkessel parameter values for each subject.

	Z [kg.m^{-4}.s^{-1}]	C [kg^{-1}.m^{4}.s^{2}]	R [kg.m^{-4}.s^{-1}]
Healthy 1	1.36×10^{7}	1.5×10^{-8}	2.28×10^{8}
Healthy 2	1.04×10^{7}	1.47×10^{-8}	1.77×10^{8}
Aneurysmal 1	1.5×10^{7}	1.05×10^{-8}	2.5×10^{8}
Aneurysmal 2	1.65×10^{7}	1.48×10^{-8}	2.77×10^{8}

APPENDIX B: Material model used for G&R

G&R kinematics

Kinematics and equilibrium equations

Nonlinear Finite-Element models based on the homogenized CMT were established and performed to simulate G&R in patient-specific ATAA [21]. Let $\boldsymbol{\chi}$: $\boldsymbol{\Omega}_0 \rightarrow \boldsymbol{\Omega}_t$ be the general mapping in a $\mathbb{R}^3$ domain between a reference configuration and a current configuration. $\boldsymbol{\Omega}_0$ is arbitrarily defined as the *in vivo* initial configuration of an artery before any insult inducing a G&R response (at homeostasis). We model the aortic wall as a mixture of different constituents, namely elastin, collagen fiber families and smooth muscle cells (SMCs). The total deformation gradient of the mixture is denoted $\mathbf{F}(\mathbf{X},t) = \frac{\partial \mathbf{x}}{\partial \mathbf{X}}$. Reference volumes $\mathrm{d}V \in \boldsymbol{\Omega}_0$ are mapped to curent volumes $\mathrm{d}v = J\mathrm{d}V \in \boldsymbol{\Omega}_t$ with the Jacobian $J = \mid \mathbf{F} \mid > 0$. Based on the CMT, we assume that all constituents in the mixture

deform together under the total deformation gradient $\mathbf{F}$ while each constituent has a different "total" deformation gradient $\mathbf{F}^i_{\text{tot}} = \mathbf{F}\mathbf{G}^i_{\text{h}}$, resulting from its own deposition stretch, $\mathbf{G}^i_{\text{h}}$, with $i \in \{\text{e}, \text{c}_j, \text{m}\}$, where superscripts e, c_j and m represent respectively the elastin, the constituent made of each of the n collagen fiber families and SMCs [38, 39]. The deposition stretch tensor of elastin may be written such as $\mathbf{G}^{\text{e}}_{\text{h}}$ = diag$[\frac{1}{\lambda^{\text{e}}_\theta \lambda^{\text{e}}_z}, \lambda^{\text{e}}_\theta, \lambda^{\text{e}}_z]$ to ensure incompressibility, with $\lambda^{\text{e}}_\theta$ and λ^{e}_z being the deposition stretches of elastin in the circumferential and longitudinal directions, respectively. The deposition stretch tensor of collagen families and SMCs may be written such as $\mathbf{G}^{\text{k}}_{\text{h}} = \lambda^k \mathbf{a}^k_0 \otimes \mathbf{a}^k_0 + \frac{1}{\sqrt{\lambda^k}}(\mathbf{I} - \mathbf{a}^k_0 \otimes \mathbf{a}^k_0)$, $k \in \{\text{c}_j, \text{m}\}$, where λ^k is the deposition stretch of the kth constituent in the fiber direction with a unit vector $\mathbf{a}^k_0$ [38, 39].

For each differential mass increment of the ith constituent deposited at time τ, the total deformation gradient of each constituent, $\mathbf{F}^i_{\text{tot}}$, is decomposed multiplicatively into an elastic part, $\mathbf{F}^i_{\text{el}}$, and an inelastic (named G&R) part, $\mathbf{F}^i_{\text{gr}}$, such as $\mathbf{F}^i_{\text{tot}} = \mathbf{F}^i_{\text{el}}\mathbf{F}^i_{\text{gr}}$ [21, 54].

Constitutive model of the aortic wall

The contribution to the mechanical behaviour of each component (elastin, four different families of collagen fibers oriented in circumferential, axial, and diagonal directions and SMCs) is captured by different strain energy density functions based on the CMT [21, 38, 39, 54]. Considering media and adventitia layers and disregarding the intima layer [21, 54], based on the mass fractions of each individual component, each specific strain energy density function may be written as

[21]:

$$W = \varrho_t^{\mathrm{e}} W^{\mathrm{e}}(\overline{I}_1^{\mathrm{e}}, J_{\mathrm{el}}^{\mathrm{e}}) + \sum_{j=1}^{n} \varrho_t^{\mathrm{c}_j} W^{\mathrm{c}_j}(I_4^{\mathrm{c}_j}) + \varrho_t^{\mathrm{m}} W^{\mathrm{m}}(I_4^{\mathrm{m}}) \tag{9}$$

where ϱ_t^i and W^i ($i \in \{\mathrm{e}, \mathrm{c}_j, \mathrm{m}\}$) refer respectively to the mass density and strain energy density of the individual constituents based on the first invariant ($\overline{I}_1^i = tr(\overline{\mathbf{C}}_{\mathrm{el}}^i)$) of the modified Cauchy-Green tensor $\overline{\mathbf{C}}_{\mathrm{el}}^i = {J_{\mathrm{el}}^i}^{-2/3}\mathbf{C}_{\mathrm{el}}^i$, on the fourth invariant ($I_4^i = \mathbf{C}_{\mathrm{el}}^i : \mathbf{a}_0^i \otimes \mathbf{a}_0^i$) of the Cauchy-Green tensor $\mathbf{C}_{\mathrm{el}}^i = {\mathbf{F}_{\mathrm{el}}^i}^{(T)}\mathbf{F}_{\mathrm{el}}^i$ and on the Jacobian ($J_{\mathrm{el}}^i = \det(\mathbf{F}_{\mathrm{el}}^i) > 0$).

The strain energy density function of elastin is described by a Neo–Hookean model in which incompressibility is enforced by a penalty term depending on the Jacobian [21] as

$$W^{\mathrm{e}}(\overline{I}_1^{\mathrm{e}}, J_{\mathrm{el}}^{\mathrm{e}}) = \frac{\mu^{\mathrm{e}}}{2}(\overline{I}_1^{\mathrm{e}} - 3) + \kappa(J_{\mathrm{el}}^{\mathrm{e}} - 1)^2 \tag{10}$$

where μ^{e} and κ are material parameters (shear and bulk modulus, respectively) with stress–like dimensions.

The strain energy density function of collagen families is assumed to write such as [39]

$$W^{\mathrm{c}_j}(I_4^{\mathrm{c}_j}) = \frac{k_1^{\mathrm{c}_j}}{2k_2^{\mathrm{c}_j}}\left[\mathrm{e}^{k_2^{\mathrm{c}_j}(I_4^{\mathrm{c}_j}-1)^2} - 1\right] \tag{11}$$

whereas the passive strain energy density for SMCs is written as

$$W^{\mathrm{m}}(I_4^{\mathrm{m}}) = \frac{k_1^{\mathrm{m}}}{2k_2^{\mathrm{m}}}\left[\mathrm{e}^{k_2^{\mathrm{m}}(I_4^{\mathrm{m}}-1)^2} - 1\right] \tag{12}$$

$k_1^{\mathrm{c}_j}$ and k_1^{m} are material parameters with stress–like dimensions while $k_2^{\mathrm{c}_j}$ and k_2^{m}

are dimensionless material parameters.

Although the same strain energy density function is used for the media and for the adventitia, both layers are distinguished by different material properties and mass densities of each individual constituent [39].

Mass turnover and G&R kinematics

Mass turnover continuously occurs by simultaneous degradation and deposition of the different microstructural constituents. This phenomenon is assumed to be a stress mediated process during which extant mass is continuously degraded and new mass is deposited into the extant matrix at a stress mediated rate [21, 54]. Therefore, the rate of mass degradation or deposition for each collagen fiber family in each layer can be expressed such as

$$\dot{\varrho}^i = \varrho_t^i k_\sigma^i \frac{\sigma^i - \sigma_{\mathrm{h}}^i}{\sigma_{\mathrm{h}}^i} + \dot{D}_{\mathrm{g}}^i \tag{13a}$$

$$k_\sigma^i = k_{\sigma 0}^i - \xi \frac{\varrho_0^{\mathrm{e}}}{\varrho_t^{\mathrm{e}}} \tag{13b}$$

where $\varrho_t^i = \varrho^i(t)$ is the mass density of the ith constituent at time t and k_σ^i stands for the corresponding growth (also named gain) parameter while σ_{h}^i and σ^i are average homeostasis and current stresses of extant fibers, respectively. $\dot{D}_{\mathrm{g}}^i$, so called the generic rate function, is used to describe additional deposition or degradation due to any damage in different constituents induced by other effects than the ones mediated by the local stress. As elastin can be only subjected to degradation, if any, and its mass loss cannot be compensated by new elastin deposition,

the following law is postulated $\dot{\varrho}^{\mathrm{e}}(t) = \dot{D}_{\mathrm{g}}^{\mathrm{e}}$ [21]. In order to couple G&R with hemodynamics effects, it is assumed in the following that the degradation rate $\dot{D}_{\mathrm{g}}^{\mathrm{e}}$ is locally scaled with the normalized RRT value ζ_{RRT}. It means that the aortic wall would undergo larger elastin degradation in regions of large RRT. This assumption, among many others which can be assessed with our computational framework, is mainly justified by recent observations suggesting that ECM proteolysis in the aortic wall could result from the advection of plasminogen across the wall [37], assuming that this advection phenomenon would be increased in regions of large RRT. Consequently, based on this assumption we considered a localized elastin degradation as an insult for G&R and simulated the subsequent ATAA progression. Accordingly, the local elastin degradation rate was written such as

$$\dot{\varrho}^{\mathrm{e}}(t) = \dot{D}_{\mathrm{g}}^{\mathrm{e}}(\mathbf{X}, t) = -\frac{\varrho^{\mathrm{e}}(\mathbf{X}, t)}{T^{\mathrm{e}}} - \zeta_{\mathrm{RRT}} \frac{D_{\mathrm{max}}}{t_{\mathrm{dam}}} \varrho^{\mathrm{e}}(\mathbf{X}, 0) e^{-\frac{t}{t_{\mathrm{dam}}}} \tag{14}$$

where t_{dam} is the temporal damage spread parameter and D_{max} is maximum damage. ζ_{RRT} is the normalized RRT defined such as: RRT/RRT$_{max}$. The first summand in Eq. 14 is a basal elastin degradation due to aging and the second summand is the elastin degradation due to abnormal RRT of blood flow.

Even when mass degradation and mass production are balanced ($\varrho_t^i = 0$), the stress–free state may change as new mass is deposited with a prestress defined according to the current configuration. Therefore, some change of the microstructure of the tissue cannot be only captured by growth contribution and so-called

remodelling was also captured by the model. Consequently, the traction–free configuration of a certain constituent was amended by both remodelling– and growth–related inelastic local changes of the microstructure and volume. For this, we employed the homogenized CMT–based G&R [21, 54]. Therefore, assuming $\mathbf{F}_{\mathrm{g}}^{i}$ and $\mathbf{F}_{\mathrm{r}}^{i}$ are inelastic deformation gradients due to G&R, respectively, the inelastic G&R deformation gradient was multiplicatively decomposed by $\mathbf{F}_{\mathrm{gr}}^{i} = \mathbf{F}_{\mathrm{r}}^{i}\mathbf{F}_{\mathrm{g}}^{i}$. The former is related to any change in the mass per unit reference volume and the latter captures changes in the microstructure due to mass turnover. Solving the following system of equations yields the evolution of the inelastic remodelling deformation gradient of the ith constituent at time t [21, 54]:

$$\left[\frac{\dot{\varrho}_{t}^{i}}{\varrho_{t}^{i}} + \frac{1}{T^{i}}\right]\left[\mathbf{S}^{i} - \mathbf{S}_{\mathrm{pre}}^{i}\right] = \left[2\frac{\partial \mathbf{S}^{i}}{\partial \mathbf{C}_{\mathrm{el}}^{i}} : (\mathbf{C}_{\mathrm{el}}^{i}\mathbf{L}_{\mathrm{r}}^{i})\right] \tag{15}$$

where $\mathbf{S}$ is the second Piola–Kirchhoff stress and subscript "pre" denotes deposition prestress while $\mathbf{L}_{\mathrm{r}}^{i} = \dot{\mathbf{F}}_{\mathrm{r}}^{i}\,\mathbf{F}_{\mathrm{r}}^{i^{-1}}$ is the remodelling velocity gradient and T^{i} is the average turnover time.

Basically local change of wall volume induced by any change in the mass of each constituent in a region of the arterial wall can be captured by the growth deformation gradient which relates the change of shape and size of a differential volume element to the degraded or deposited mass in that element. Based on the homogenized CMT, it is suggested that all constituents experience the same inelastic growth deformation gradient: $\mathbf{F}_{\mathrm{g}}^{i} = \mathbf{F}_{\mathrm{g}}$ [21, 54]. Assuming $\mathbf{a}_{\mathrm{g}}^{i}$ is a unit vector denoting the growth direction of individual constituents and $\varrho_{t}^{tot} = \sum_{i=1}^{n} \varrho_{t}^{i}$

is the total volumic mass at each time. The total inelastic growth deformation gradient rate was eventually written such as:

$$\dot{\mathbf{F}}_{\mathrm{g}} = \sum_{i=1}^{n} \frac{\dot{\varrho}_t^i}{\varrho_t^{tot} \left[\mathbf{F}_{\mathrm{g}}^{i\,-\mathrm{T}} : \mathbf{a}_{\mathrm{g}}^i \otimes \mathbf{a}_{\mathrm{g}}^i \right]} \mathbf{a}_{\mathrm{g}}^i \otimes \mathbf{a}_{\mathrm{g}}^i \tag{16}$$